


Rosette Trajectories Enable Ungated, Motion-Robust, Simultaneous Cardiac and Liver T_2^* Iron Assessment

Adam M. Bush, PhD,^{1*}  Christopher M. Sandino, MS,² Shreya Ramachandran, BS,³ Frank Ong, PhD,¹ Nicholas Dwork, PhD,⁴ Evan J. Zucker, MD,¹ Ali B. Syed, MD,¹ John M. Pauly, PhD,² Marcus T. Alley, PhD,¹ and Shreyas S. Vasanawala, MD, PhD¹

Background: Quantitative T_2^* MRI is the standard of care for the assessment of iron overload. However, patient motion corrupts T_2^* estimates.

Purpose: To develop and evaluate a motion-robust, simultaneous cardiac and liver T_2^* imaging approach using non-Cartesian, rosette sampling and a model-based reconstruction as compared to clinical-standard Cartesian MRI.

Study Type: Prospective.

Phantom/Population: Six ferumoxytol-containing phantoms (26–288 $\mu\text{g/mL}$). Eight healthy subjects and 18 patients referred for clinically indicated iron overload assessment.

Field Strength/Sequence: 1.5T, 2D Cartesian and rosette gradient echo (GRE)

Assessment: GRE T_2^* values were validated in ferumoxytol phantoms. In healthy subjects, test–retest and spatial coefficient of variation (CoV) analysis was performed during three breathing conditions. Cartesian and rosette T_2^* were compared using correlation and Bland–Altman analysis. Images were rated by three experienced radiologists on a 5-point scale.

Statistical Tests: Linear regression, analysis of variance (ANOVA), and paired Student's *t*-testing were used to compare reproducibility and variability metrics in Cartesian and rosette scans. The Wilcoxon rank test was used to assess reader score comparisons and reader reliability was measured using intraclass correlation analysis.

Results: Rosette $R2^*$ ($1/T_2^*$) was linearly correlated with ferumoxytol concentration ($r^2 = 1.00$) and not significantly different than Cartesian values ($P = 0.16$). During breath-holding, ungated rosette liver and heart T_2^* had lower spatial CoV (liver: $18.4 \pm 9.3\%$ Cartesian, $8.8\% \pm 3.4\%$ rosette, $P = 0.02$, heart: $37.7\% \pm 14.3\%$ Cartesian, $13.4\% \pm 1.7\%$ rosette, $P = 0.001$) and higher-quality scores (liver: 3.3 [3.0–3.6] Cartesian, 4.7 [4.1–4.9] rosette, $P = 0.005$, heart: 3.0 [2.3–3] Cartesian, 4.5 [3.8–5.0] rosette, $P = 0.005$) compared to Cartesian values. During free-breathing and failed breath-holding, Cartesian images had very poor to average image quality with significant artifacts, whereas rosette remained very good, with minimal artifacts ($P = 0.001$).

Data Conclusion: Rosette *k*-sampling with a model-based reconstruction offers a clinically useful motion-robust T_2^* mapping approach for iron quantification.

J. MAGN. RESON. IMAGING 2020.

T_2^* IS A CLINICALLY USEFUL BIOMARKER for tissue iron quantification.^{1,2} In vivo, endogenous paramagnetic compounds like hemosiderin and ferritin cause

microscopic field inhomogeneity and increase local T_2^* -related dephasing³; thus, quantitative T_2^* can be used to spatially determine tissue-specific iron content.

View this article online at wileyonlinelibrary.com. DOI: 10.1002/jmri.27196

Received Feb 11, 2020, Accepted for publication May 1, 2020.

*Address reprint requests to: A.M.B., 350 Serra Mall, Stanford, CA, 94305. E-mail: adambush@stanford.edu

Contract grant sponsor: NIH; Contract grant numbers: R01EB009690, NIH R01EB026136, R01DK117354, NHLBI 5T32EB009035; Contract grant sponsor: GE Healthcare

Level of Evidence: 1Technical Efficacy Stage: 1

From the ¹Department of Radiology, Stanford University, Palo Alto, California, USA; ²Department of Electrical Engineering, Stanford University, Palo Alto, California, USA; ³Department of Electrical Engineering and Computer Science, University of California, Berkeley, California, USA; and ⁴Department of Radiology and Biomedical Imaging, University of California, San Francisco, California, USA

Additional supporting information may be found in the online version of this article

Iron overload, resulting from excess iron accumulation in hereditary hemochromatosis and transfusion-dependent patients, may lead to organ failure and death. Historically, liver biopsy was the gold standard method for body iron quantification and chelation management; however, procedural complication risk, sampling errors, and low patient tolerance have limited enthusiasm for this method.⁴ T_2^* magnetic resonance imaging (MRI) offers a noninvasive, accurate, repeatable, and well-tolerated method to assess iron in various organs, including the liver, heart, kidneys, spleen, and pancreas.⁵ As a result, iron assessment by MRI has replaced liver biopsy as the clinical standard, guiding patient management and enhancing patient survival; further, it has enabled research into basic iron loading mechanisms.⁶ Today, cardiac-iron related mortality has been essentially eliminated in well-managed patients.⁷

However, despite the success of MR iron assessment, there are several remaining challenges. First, quantification and image quality of existing T_2^* techniques are easily corrupted by motion,⁴ limiting clinical utility in pediatric patients. Typically, motion artifacts are minimized by breath-holding and/or gating strategies that “freeze” respiratory and cardiac motion. Unfortunately, these strategies are inherently inefficient, prolonging scan times. Particularly in pediatric populations, sedation is common, adding risk and expense.⁸ Second, comprehensive iron assessment requires both cardiac and liver T_2^* quantification due to disparate iron loading

phenotypes.⁹ Although liver iron is an excellent marker of total body iron, cardiac iron is the strongest prognostic marker of mortality and does not correlate well with liver iron.^{10,11} Furthermore, practical challenges including large scan coverage, receive coil placement, and differing motion compensation schemes¹² have prevented simultaneous cardiac/hepatic acquisitions, leading to long clinical exams.⁴ Although previous work has sought to address these concerns with the use of novel motion compensation strategies and simultaneous liver and cardiac T_2^* imaging,^{13,14} these approaches have yet to become a part of routine clinical iron exams.

One successful motion-robust approach entails non-Cartesian data sampling strategies such as radial and spiral, as they yield diffuse aliasing artifacts and their frequent sampling of the center of k -space reduces noise.¹⁵ Furthermore, non-Cartesian acquisitions are well suited for compressed sensing and other model-based reconstructions that can further reduce motion artifacts.¹⁶ Although non-Cartesian sampling is usually described for single echo scans, non-Cartesian strategies for multiecho brain fMRI¹⁷ and body fat quantification have been successfully implemented.¹⁸ Despite this success, no work to date has explored the utility of non-Cartesian imaging for quantitative body T_2^* iron assessment, particularly in the heart.

Rosettes are non-Cartesian, flower-like k -space trajectories, first described by Noll¹⁹ and categorized by Li et al.²⁰ Previous and ongoing in vivo work using rosette sampling has focused on low-resolution, spectroscopic imaging due to the off-resonance, deconstructive interference property of rosette trajectory self-crossings.²¹ Although the off-resonance sensitivity is advantageous in spectroscopic imaging, in most other applications off-resonance degrades image quality, as it leads to both blurring and signal dropouts, characteristic of rosette imaging.¹⁹ Much prior work has focused on off-resonance correction of non-Cartesian trajectories^{22,23} and one successful approach involves a segmented k -space reconstruction.²³

Therefore, the goal of this work was to develop and evaluate a motion-robust, simultaneous cardiac and liver T_2^* imaging approach using non-Cartesian, rosette sampling and a model-based reconstruction as compared to clinical-standard, Cartesian MRI.

TABLE 1. Imaging Parameters Used in Cartesian and Rosette Multiecho, Gradient Echo Pulse Sequences

Parameter	Cartesian	Rosette
Gating	ECG/PPG gated	Ungated
Matrix size	256 × 256	512 × 512
FOV (cm)	40	50
Resolution (mm)	1.5	1
Slice thickness (mm)	8	8
Flip angle (deg)	25	15
Repetition time (msec)	15.7	18
Echo times (msec)	1.1, 2.4, 3.7, 5.0, 6.3, 7.6, 8.9, 10.2	0.8, 4.6, 7.6, 10.6, 13.6
Scan time (second)	15–20	15

Materials and Methods

All studies were performed at Lucile Packard Children’s Hospital at Stanford University, with Institutional Review Board (IRB) approval and informed consent and assent of all subjects.

Imaging was performed on a GE Signa 450W MRI system with a 20-channel cardiac coil (GE Healthcare, Waukesha, WI). Cartesian and rosette imaging parameters are found in Table 1. For Cartesian scans, a cardiac-gated, multiecho gradient echo, (GRE) sequence was used with the eight echoes, initial echo time (TE) 1.1 msec, echo spacing of 1.3 msec, and trigger delay of 10 msec. Other

sequence parameters include flip angle 25° , repetition time (TR) 15.7 msec, 40 cm field of view, 1.5 mm in-plane resolution, and 8 mm slice thickness. ECG gating was used in patients, whereas peripheral gating was used in healthy volunteer scans. A total of 10–16 views per segment were used to keep the scan time between 15–20 seconds, depending on heart rate.

For rosette scans, we extended the work of Noll¹⁹ and Li et al²⁰ and defined Class II rosettes as follows:

$$\begin{aligned} \text{if } N \text{ is odd, } q &= \left\{ \frac{N+2}{N} + \frac{2(k-1)}{N}, k \in \mathbb{Z}^+ \right\}, \{Z^+\} \\ \text{if } N \text{ is even, } q &= \left\{ \frac{N+2}{N} + \frac{4(k-1)}{N}, k \in \mathbb{Z}^+ \right\}, \{Z^+\} \end{aligned} \quad (1)$$

where k is an incrementing parameter, N is the number of petals, and q is a shape parameter defined as ω_2/ω_1 , where ω_1, ω_2 are rotational frequencies defined in the original rosette formulation.¹⁹

In our approach, a single repetition, or flower, is segmented into multiple echoes, or petals (Fig. 1a,d) defined as the trajectory sampling window centered around each k -space center crossing. Each flower is then rotated by a golden angle (137.5°) (Fig. 1b,e) to ensure adequate sampling and that various motion states are evenly distributed throughout k -space.²⁴ By grouping similarly timed petals across shots, a multiecho dataset is achieved (Fig. 1f).

Imaging Parameters

For the rosette sequence, a 15° flip angle, a TR of 18 msec, and q value of 2.2 were chosen with a total readout duration of 16 msec.

The sequence was constrained to a maximum slew rate of 75 mT/m/s and gradient amplitude of 40 mT/m to reduce eddy current and gradient timing-related artifacts. Trapezoidal waveforms were used to convert the analytical gradients into physical gradient achievable on the scanner and return to the k -space center at the end of readout for an improved steady-state condition. The rosette gradient waveforms are depicted in Fig. 1c. Both radiofrequency and gradient spoiling were performed. A total of 800 continuous repetitions were performed, each rotated by 137.5° for a comfortable breath-hold scan time of 15 seconds. The 800 repetitions were grouped into five unique echo times based on k -space center crossing times, of 0.8, 4.6, 7.6, 10.6, and 13.6 msec. A cardiac self-gated reconstruction with a 300 msec window 200 msec following peak systole and an ungated time-averaged reconstruction using all temporal cardiac samples were performed²⁵ (Fig. 2).

Gradient Delay Correction

Prior to image reconstruction, a gradient delay correction was performed on the nominal rosette gradient waveforms to correct for hardware imperfections due to gradient switching.⁴ A simple, retrospective, bulk gradient delay time constant was empirically determined for each physical gradient axis²⁶ using a ferumoxytol phantom. An exhaustive search approach was used to determine the ideal physical gradient delay on each gradient axis based on closeness of the Cartesian and rosette T_2^* values. Patient-specific delay correction was performed by interpolating the nominal gradient waveforms and applying the appropriate patient-specific rotation matrix, delaying the physical gradients along x , y , and z and rotating back

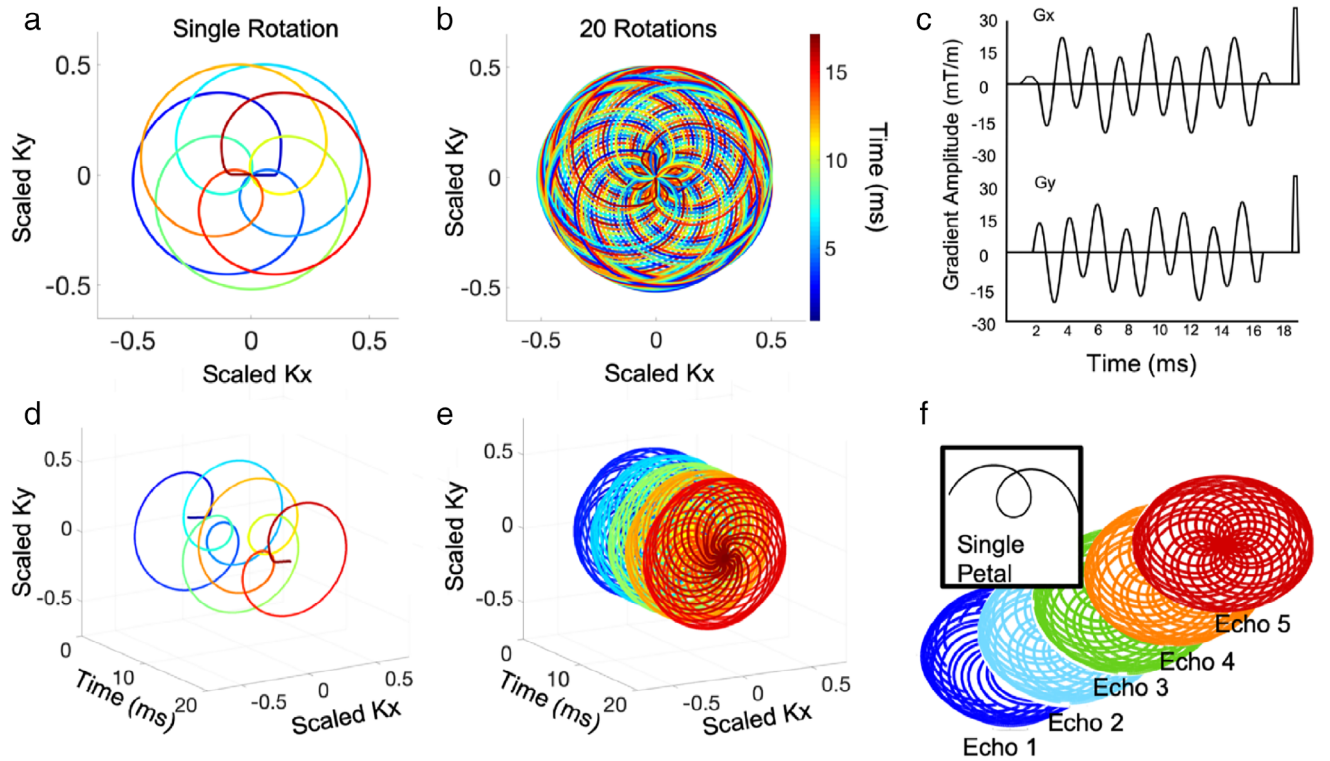


FIGURE 1: A single, $q = 2.2$ rosette repetition, or flower, where the colors correspond to the effective echo time in k -space (a) and kt -space (d). By rotating the nominal rosette flower by the golden angle (137.5°), k -space (b) and kt -space (e) are adequately sampled. Separating each rosette flower into individual petals defined by the k -space center crossing allows for a multiecho data acquisition (f). The corresponding readout gradient and spoiling gradient waveforms are also shown (c)

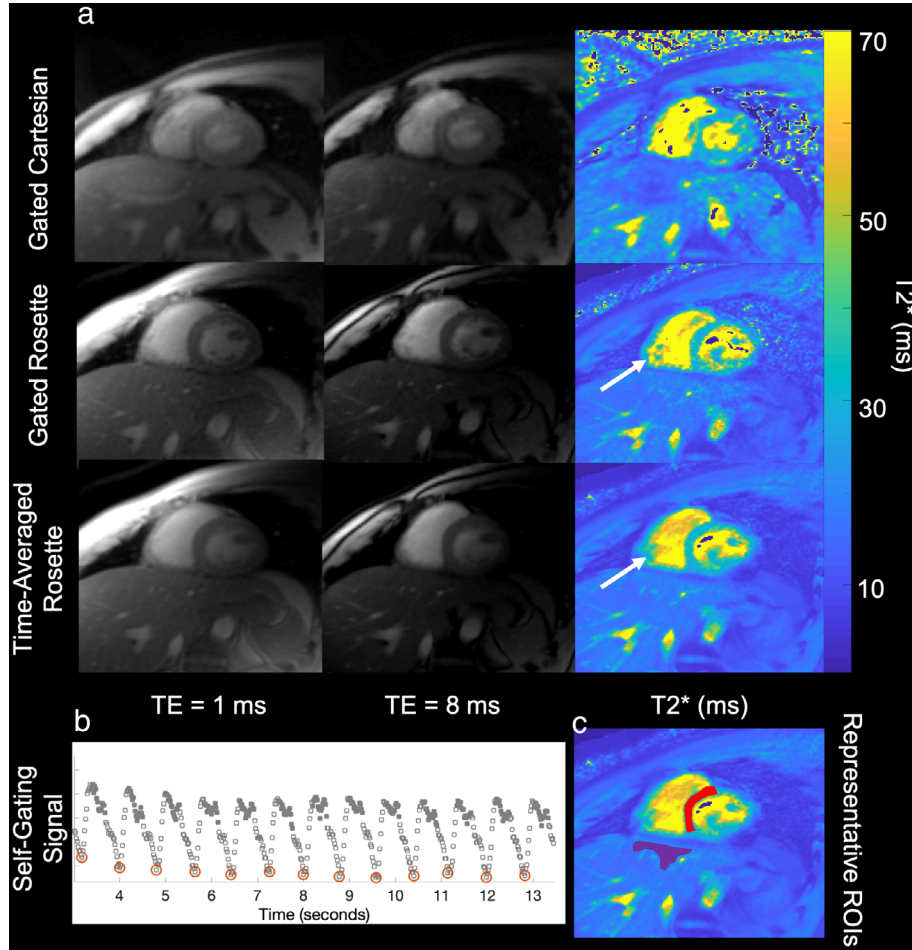


FIGURE 2: (a) Representative single-echo images at two echo times and T_2^* maps of the gated Cartesian (TE = 1.3 and 7.6 msec), retrospectively self-gated rosette, and time-averaged rosette (TE = 0.8 and 7.6 msec) in a mid, short axis slice. Although clear delineation exist between the septum and blood pool, the white arrows show temporal blurring of the papillary muscles in a time-averaged T_2^* map. (b) The rosette trajectory starts from the center of k -space and can be used to create a self-gating magnitude signal that encodes cardiac motion. The open squares correspond to every repetition, red open circles correspond to peak systole, and gray filled squares correspond to repetitions used in a self-gated reconstruction. (c) The hepatic (purple) and myocardial septal (red) regions of interests are shown

onto the nominal coordinate frame to obtain the delayed k -trajectory.

Image Reconstruction

A parallel imaging reconstruction with locally low-rank regularization was used.²⁷ The reconstructed images are produced by iteratively solving the following optimization problem:

$$\arg \min_x \|y - FSx\|_2^2 + \lambda \|C(x)\|_* \quad (2)$$

where the reconstructed images, x , were transformed into the raw k -space data (y) using a signal model comprised of coil sensitivity maps (S) and the nonuniform Fourier transform operator (F). Coil sensitivity maps were derived using ESPIRiT (Eigenvalue iTerative Self-consistent Parallel Imaging Reconstruction) from a gridded reconstruction of the first 32 k -space samples of the initial echo.²⁸ An empirically determined regularization parameter (λ) of 0.0001 was used. A locally low rank constraint was integrated by minimizing

the nuclear norm of a Casorati matrix, $C(x)$, whose columns are comprised of patches from different spatial locations in the image. To reduce the computational complexity of each iteration, raw data were coil-compressed using principal component analysis.²⁹ All reconstruction code was implemented using the Berkeley Advanced Reconstruction Toolbox (BART).³⁰ Magnitude, voxelwise mono-exponential fitting was performed using custom Python scripts to calculate spatial T_2^* maps, and truncation was performed in cases of exceptionally short T_2^* for improved robustness.³¹

Phantom Imaging

Six phantoms containing distilled water, 2% carrageenan by mass,³² and variable concentrations of ferumoxytol³³ (26, 36, 72, 120, 168, 288 $\mu\text{g/mL}$) were constructed. The T_2^* phantoms were submerged in a room temperature water bath to limit susceptibility artifacts. Cartesian and rosette multiecho images were acquired in an axial orientation.

In Vivo Imaging

The reproducibility and motion sensitivity experiments were performed in eight healthy volunteers (seven male, 26.7 ± 4.2 years), whereas accuracy experiments were performed in the healthy volunteers and 18 additional subjects undergoing clinically indicated T_2^* iron assessment (17 transfusion-induced iron overload, one hereditary hemochromatosis, 10 male, 17.7 ± 6.0 years). All in vivo images were acquired in a single slice, mid-ventricle, short-axis orientation.

Image quality was rated by three radiologists (S.V., 19 years experience, E.Z., 8 years experience, A.S., 5 years experience) blinded to imaging technique on the following 5-point scale¹²: 1: Very poor, unusable images; 2: Average image quality with significant artifacts; 3: Good image quality with moderate artifacts; 4: Very good quality with minimal artifacts; 5: Excellent image quality with no significant artifacts. Image quality assessment of the liver and myocardial septum was performed on all Cartesian and rosette T_2^* maps. A composite mean and standard deviation score across reviewers was calculated. Manual regions of interest were drawn in the myocardial septum, encompassing epicardial and endocardial borders³⁴ and the dome of the liver, with attention to avoid hepatic vessels (Fig. 2).

Reproducibility experiments consisted of three breath-hold Cartesian and rosette acquisitions separated by less than 20 minutes. Test–retest coefficient of variation (CoV_{RT}) was calculated as the mean divided by the standard deviation of the three scans and represented a measure of T_2^* reproducibility. The spatial coefficient of variation (CoV_s) for each T_2^* map was also calculated as the mean of voxel measurements in a region of interest divided by the standard deviation and was a measure of spatial uniformity in the T_2^* maps. The motion-related error in T_2^* was calculated as the difference in free-breathing and incomplete breath-hold T_2^* from breath-hold T_2^* .

Motion sensitivity was assessed by comparing free breathing and failed breath-hold T_2^* scans in the same eight healthy subjects. During the failed breath-hold, volunteers were instructed to hold their breath for the first 5–10 seconds and then resume normal tidal breathing for the remainder of the scan. The image quality scores, CoV_s , and the absolute, average error between the breathing maneuvers and breath-hold test–retest T_2^* results were calculated as metrics of motion sensitivity.

Statistical Tests

The linear correlation r^2 and limits of agreement of phantom $R2^*$ values and ferumoxytol concentration with and without gradient delay correction was measured.³³ Analyses of variance (ANOVAs) for T_2^* , CoV_{RT} , and CoV_s values were performed across breath-hold Cartesian, gated rosette, and time-averaged rosette conditions to measured motion sensitivity. On statistically significant comparisons via ANOVA, multiple Student's t -tests with Tukey correction were performed. Paired Student's t -test was used to compare Cartesian to time-averaged rosette T_2^* , T_2^* error, CoV_{RT} , and CoV_s values in both free-breathing and incomplete breath-hold conditions. A paired Student's t -test with Dunnett correction was used to compare breath-hold T_2^* , CoV_{RT} , and CoV_s values to free breathing and incomplete breath-hold values in Cartesian and rosette scans. Linear correlation r^2 and limits of agreement between Cartesian and

rosette T_2^* values were calculated in all breath-hold scans and used as a measure of accuracy. Two-way mixed, consistency intraclass correlation coefficient, and the 95% confidence interval was determined for image score reader reliability. Medians and interquartile ranges of the composite mean reader scores were calculated and compared using Wilcoxon rank sum test or Kruskal–Wallis test followed by Steel–Dwass correction for multiple comparisons. $P < 0.05$ was considered significant. Statistical analysis was performed JMP Pro 14 (SAS, Cary, NC).

Results

Our rosette formalism produced a wide range of echo spacings compared to prior definitions (Fig. S1). Higher petal and/or k -values resulted in variable density sampling³⁵ with higher average gradient amplitudes at peripheral, high k -spatial frequencies and lower average gradient amplitudes at central, low k -spatial frequencies.

Phantom Imaging

The carrageen, ferumoxytol phantom produced a stable gelatinous phantom across the clinically relevant range of T_2^* values. Prior to gradient delay correction, the measured rosette $1/T_2^*$ ($R2^*$) was linearly correlated with ferumoxytol concentration up to $288 \mu\text{g/mL}$ ($r^2 = 0.999$) but was systematically underestimated relative to the Cartesian T_2^* values by $-13.4\% \pm 5.8\%$ ($P = 0.002$). A gradient delay of $2.4 \mu\text{s}$ in the x and y direction and a $0.6 \mu\text{s}$ delay in the z direction reduced the observed T_2^* underestimation to $-2.8\% \pm 4.2\%$ ($P = 0.16$) (Fig. S2) and was applied retrospectively to all rosette scans. Example images before and after the gradient delay correction are shown in Fig. S3, demonstrating improved spatial homogeneity of T_2^* mapping.

In Vivo Imaging

In eight healthy subjects, the average liver T_2^* was 24.6 ± 4.2 msec, 25.1 ± 3.1 msec, and 24.0 ± 3.6 msec (ANOVA $P = 0.92$), while the average myocardial T_2^* was 34.9 ± 3.3 msec, 31.9 ± 2.2 msec, and 32.0 ± 2.6 msec (ANOVA $P = 0.09$) for the Cartesian, self-gated rosette, and time-averaged rosette, respectively, and were not statistically different.

CoV_{RT} , CoV_s , and quality scores for all breathing conditions can be found in Table 2. There was no statistical difference in breath-hold T_2^* CoV_{RT} between Cartesian, self-gated, and time-averaged measurements in the liver (ANOVA, $P = 0.48$) nor the myocardial septum (ANOVA, $P = 0.51$). Between Cartesian, self-gated rosette, and time-averaged rosette, there was a statistical difference in liver and heart CoV_s (ANOVA, liver $P = 0.006$, heart $P < 0.001$) and image quality (Kruskal–Wallis, liver $P = 0.01$, cardiac $P = 0.002$). Image quality was rated statistically the highest and CoV_s statistically the lowest in the time-averaged breath-hold acquisitions for both the liver and myocardium; details

TABLE 2. Image Variability and Quality Statistics for Gated Cartesian, Self-Gated Rosette, and Time-Averaged Rosette During Different Various Breathing Conditions

Parameter		Cartesian	Self-gated rosette	Time-averaged rosette
T₂* variability				
Liver	CoV TRT breath-held	7.8 ± 9.7%	3.9 ± 4.0%	3.6 ± 2.3%
	CoV spatial breath-held	18.4 ± 9.3%	19.9 ± 5.6%	8.8 ± 3.4%** ⁺⁺
	CoV spatial free-breathing	59.1 ± 73.3%		9.3 ± 3.3%
	CoV spatial failed breath-hold	82.6 ± 78.9%		11.9 ± 5.9%*
	% Error from free-breathing	18.4 ± 15.6%		9.9 ± 6.9%
	% Error from failed breath-hold	24.5 ± 28.2%		15.4 ± 10.8%
Cardiac	CoV TRT breath-held	4.6 ± 3.1%	4.0 ± 1.7%	3.3 ± 1.2%
	CoV spatial breath-held	37.7 ± 14.3%	21.2 ± 5.6%*	13.4 ± 1.7%** ⁺⁺
	CoV spatial free-breathing	62.5 ± 24.6%		13.7 ± 3.0%**
	CoV spatial failed breath-hold	82.3 ± 28.0%		14.7 ± 2.4%**
	% Error from free-breathing	15.7 ± 10.2%		3.7 ± 2.3%*
	% Error from failed breath-hold	42.4 ± 36.8%		7.3 ± 10.6%*
Image quality				
Liver	Breath held	3.3 [3–3.6]	4.2 [3.5–4.6]	4.7 [4.1–4.9]**
	Free-breathing	2 [1.7–2.3]		4.3 [3.8–4.3]**
	Failed breath-hold	2 [1.3–2.7]		3.8 [3.0–4.2]**
	Interreader ICC (%)	91.6 [82.7–96.3]%		90.7 [80.8–95.9]%
Cardiac	Breath-held	3.0 [2.3–3]	4.0 [3.3–4.6]*	4.5 [3.8–5.0]**
	Free-breathing	2.0 [1.7–2.3]		4.5 [3.6–4.7]**
	Failed breath-hold	1.3 [1.0–2.3]		3.8 [2.8–4.3]**
	Interreader ICC (%)	73.2 [59.1–83.4]%		91.3 [82.7–96.3]%*

*Statistically different from Cartesian (**P* < 0.05, ***P* < 0.005). +Statistically different from self-gated rosette (+*P* < 0.05, ++*P* < 0.005). ICC = intraclass correlation coefficient.

can be found in Table 2. Since the time-averaged rosette was noninferior to gated rosette images in terms of accuracy and demonstrated lower spatial variability, and superior quality scores, only time-averaged rosette reconstructions were analyzed further.

Image quality and variability estimates during free-breathing and failed breath-hold conditions are shown in Fig. 3 along with representative T₂* maps. In Cartesian T₂* maps, the liver CoV_s was statistically larger during free-breathing than breath-hold (*P* = 0.04) and the myocardial CoV_s was statistically larger during free-breathing (*P* = 0.008) and incomplete breath-holding (*P* = 0.002) than breath-hold scans. However, there was no statistical pairwise difference in liver or myocardial CoV_s in free-breathing or incomplete

breath-holding compared to breath-hold values (all above *P* > 0.05) (Table 2).

Additionally, in the liver the average error in T₂* induced by the breathing motion was not statistically different from breath-holding for free breathing (*P* = 0.20) or for incomplete breath-holding scans (*P* = 0.20). However, in the heart the average error in T₂* from breathing motion was larger in free-breathing Cartesian (*P* = 0.006) and incomplete breath-holding Cartesian (*P* = 0.03) than rosette scans (Table 2).

The median and interquartile ranges of the average image quality scores can be found in Table 2. Across all breathing conditions and anatomical locations rosette T₂* map quality was rated better than Cartesian image quality

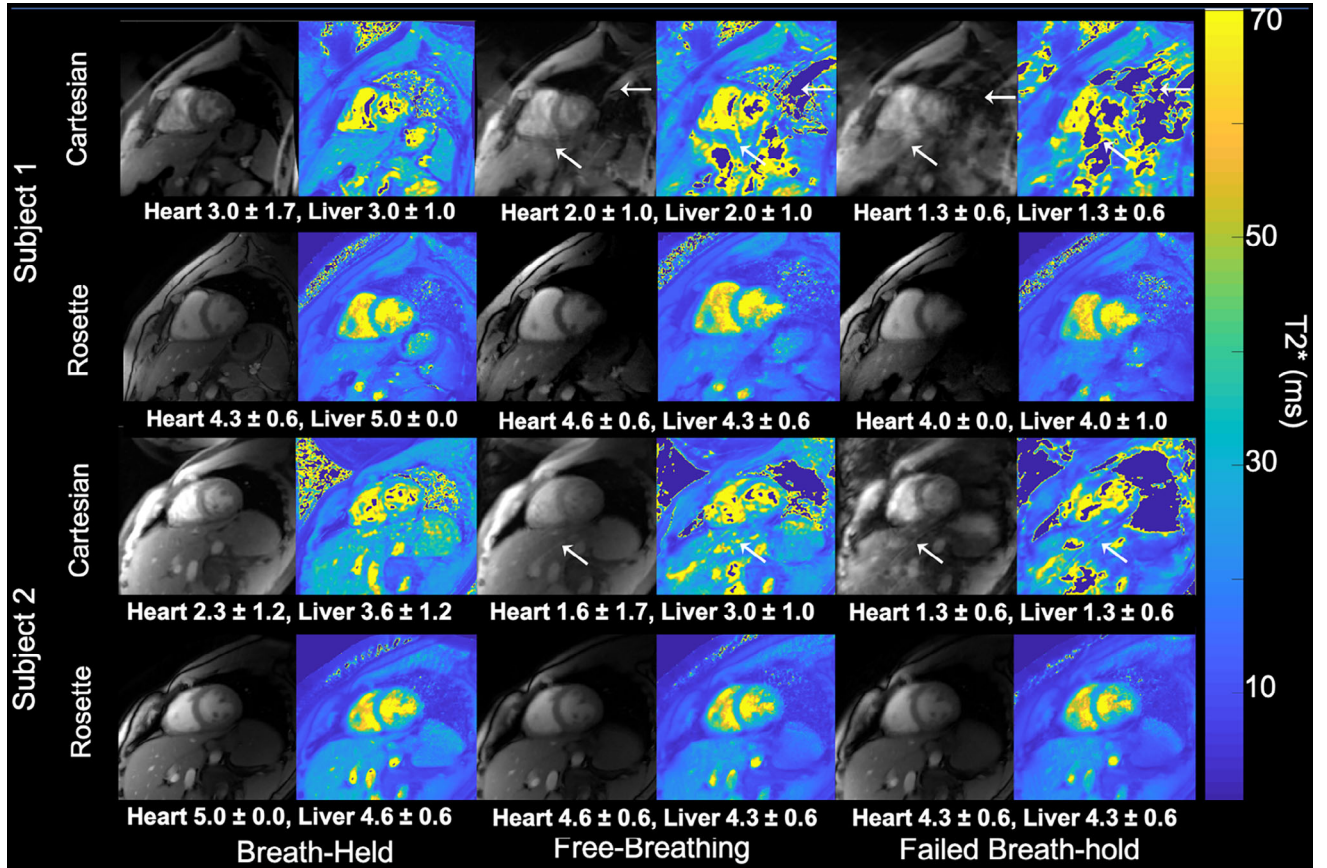


FIGURE 3: In two representative subjects, gated Cartesian and time-averaged rosette individual echo ($TE = 7.6$, gray scale) and T_2^* maps, with image quality scores below each map, are shown under three different breathing conditions: breath-hold, free-breathing, and failed breath-holding. Diffuse motion-induced aliasing artifacts in individual echoes (white arrows) produce large data corrupting artifacts in gated Cartesian T_2^* maps (white arrows). Conversely, rosette reconstructions are largely immune to these artifacts and excellent global image quality and myocardium-blood pool delineation is seen in all images

($P < 0.005$) (Table 2). In Cartesian acquisitions, T_2^* map image quality was rated as significantly lower during both free-breathing (liver $P = 0.021$, cardiac $P = 0.010$) and failed breath-holding (liver $P = 0.002$, cardiac $P = 0.009$). Conversely, rosette free-breathing image quality scores were not significantly different from breath-held scans (liver $P = 0.093$, cardiac $P = 0.67$). Although failed breath-holding scores were lower in the liver (liver $P = 0.036$, cardiac $P = 0.06$) they were still rated as “very good” (Table 2). Interrater intraclass coefficient reliability in the liver was excellent and statistically similar between Cartesian and rosette rated T_2^* maps ($P = 0.96$). However, interrater intraclass coefficient reliability in the heart was only acceptable in the Cartesian and remained excellent in rosette rated T_2^* maps ($P = 0.01$).

Cartesian vs. rosette T_2^* was measured in 26 subjects (eight healthy subjects and 18 patients undergoing clinical iron quantification) (Fig. 4). Rosette T_2^* systematically underestimated Cartesian T_2^* as the average paired difference in rosette and Cartesian liver T_2^* was -1.3 ± 0.3 msec ($P < 0.001$) and myocardial T_2^* was -3.5 ± 1.2 msec ($P < 0.001$). Correlation of rosette and Cartesian T_2^* was excellent in the liver ($r^2 = 0.98$, $P < 0.001$) and weak but

significant in the myocardium ($r^2 = 0.33$, $P = 0.006$) (Fig. 5). Across all subjects, the absolute pairwise difference in CoV_s was higher in Cartesian compared to rosette images by $6.9\% \pm 2.3\%$ ($P = 0.005$) in the liver and by $22.1\% \pm 5.1\%$ ($P < 0.001$) in the myocardium.

Discussion

We introduced a method for T_2^* quantification using rosette k -space sampling and a model-based reconstruction. This approach produced comparable T_2^* quantification with superior image quality, higher spatial resolution, fewer motion artifacts, and reduced spatial variability without gating in a similar scan time as compared to the clinical standard technique. Rosette multiecho imaging offers several practical advantages over traditional approaches.

First, in equal scan time, rosette T_2^* imaging had similar accuracy and reproducibility and better base image quality and resolution when compared to traditional methods. Since T_2^* imaging is used longitudinally to follow chelation efficacy, high reproducibility and accuracy is critical in clinical iron management. Rosette imaging demonstrated comparable

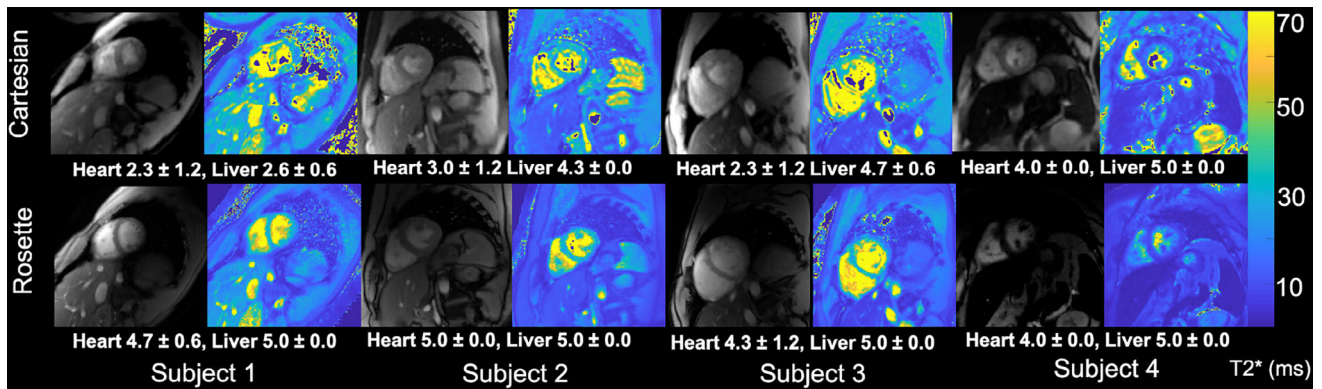


FIGURE 4: Representative images from four of the 18 patients undergoing clinical iron examination with gated Cartesian (top row) and time-averaged rosette (bottom row) echo images (TE = 7.6 msec, grayscale) and T_2^* maps (color maps) are shown with corresponding image quality scores below

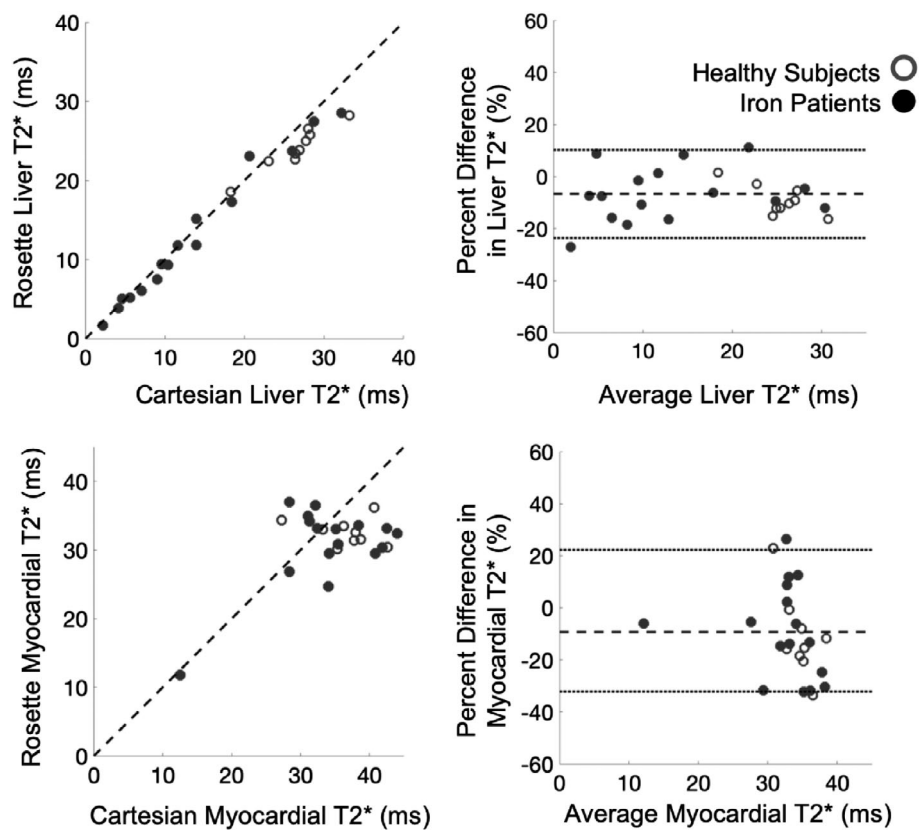


FIGURE 5: Correlation (left) and Bland–Altman (right) plots in the gated Cartesian vs. time-averaged rosette T_2^* quantification in the liver (top) and myocardial septum (bottom) for healthy subjects (open circles) and patients referred for iron assessment (closed circles). Unity lines are shown as the dashed line in correlation plots. Liver results showed high agreement across the entire T_2^* range, with a mean bias of -5.1% and 95% confidence interval, limits of agreement of 9.3% to -21.9% . The gated Cartesian and time-averaged rosette myocardial septum results were more discordant, with a mean bias of -8.4% and 95% confidence interval, limits of agreement of 21.4% to -32.1%

precision and accuracy in phantoms. In subjects, the liver and cardiac CoVT_RT trended lower than Cartesian but was not statistically significant and agreed well with previously reported data.³⁶ Furthermore, the liver T_2^* displayed high accuracy across the entire physiologic range. Although we observed deviations in myocardial T_2^* measurements relative to Cartesian measurements, our cohort had only one subject

with excess myocardial iron, a relatively rare condition. The Bland–Altman agreement in Cartesian and rosette myocardial T_2^* was comparable to previous reports¹⁴ and the variance is most likely due to the high variability of the clinical standard, Cartesian T_2^* technique in the healthy T_2^* range.

Traditional bright blood T_2^* mapping is known to be variable in healthy subjects.³⁷ Furthermore, we measured

higher spatial variability, lower reader scores, and observed poor myocardium-blood pool differentiation in the Cartesian T_2^* than rosette T_2^* maps of this study. The improvements in image quality are clinically important, as poor image quality reduces clinical confidence in the quantification, resulting in frequent repeat scans and even sedation. Furthermore, although variability in regional iron deposition has been observed in excised hearts, low spatial resolution, high spatial variability, and lower reader confidence in Cartesian T_2^* maps have made it difficult to examine in vivo.³⁸ Therefore, precise, accurate, and high-resolution rosette T_2^* mapping is a promising and powerful clinical and research tool.

Another advantage of rosette T_2^* imaging is high spatiotemporal reproducibility without cardiac gating. The ungated, time-averaged rosette T_2^* maps displayed higher image quality and comparable test–retest reproducibility to a cardiac gated rosette, cardiac gated Cartesian, and literature T_2^* maps in both the liver and myocardium.³¹ By leveraging the additional data from a continuous acquisition across all cardiac phases, the incoherent aliasing artifacts of non-Cartesian rosette acquisitions and the denoising properties of an iterative locally low rank reconstruction, cardiac gating was unnecessary for the generation of reliable and accurate T_2^* maps, with superior image quality to the clinical standard approach. In the clinical setting, ungated acquisitions are preferable because patient motion, ECG triggering failure, and variable and/or high heart rates often confound imaging protocols and reduce diagnostic confidence.

Finally, respiratory gating was not needed for high image quality and reader confidence in liver and myocardial T_2^* estimation. Cartesian T_2^* maps were markedly corrupted by respiratory motion; however, rosette T_2^* imaging was largely unaffected. Clear motion-induced ghosting can be seen in source Cartesian images at various echo times, which contributes to large errors in T_2^* estimates, poor map quality, and higher spatial variability in both the liver and the heart. On the other hand, rosette images were largely unaffected by respiratory motion, which translated to minimal errors in T_2^* , negligible loss of map quality, and no increase in spatial variability for both the heart and liver. Clinically, failed and incomplete breath-holding are commonly encountered in pediatric patients resulting in poor T_2^* assessment, sedation, repeat scan, and even repeats visits. Therefore, ungated motion-robust rosette T_2^* assessments are not only faster and more reliable, but also improve patient tolerance and safety.

This work is an extension of much prior work involving rosette trajectories,^{19,20} non-Cartesian multiecho imaging,^{17,18} and motion-robust T_2^* mapping approaches.^{12,14} In particular, previous quantitative, motion-robust T_2^* mapping strategies have used single acquisitions and nonrigid motion correction to achieve improved image quality in the presence of motion.^{12,14} Although successful, our approach has the additional benefit of requiring no patient-specific motion

correction, being completely ungated and having identical scan times to the clinical standard while achieving higher spatial resolution.

Limitations

Despite the major improvements of ungated, rosette T_2^* images over the conventional approach, this work is not without limitations. First, our study was conducted in a limited number of subjects, which increases the likelihood of type II statistical error, especially with respect to the variability and motion sensitivity parameters. Despite this limitation, we conclusively demonstrate that rosette T_2^* maps produced quantitatively similar reproducibility and accuracy, lower variability, and higher-quality images. Next, non-Cartesian sampling trajectories are more susceptible to gradient timing-related imperfections that can influence image quality and quantitation. Although we address some of these effects by tempering the slew rate and applying a simple retrospective gradient delay correction, patient-specific and prospective methods should be explored in the future.¹⁸ Gradient timing errors manifest as both magnitude and phase errors, which can lead to T_2^* estimation errors.³⁹ Many strategies have been proposed to correct for gradient timing artifacts, including direct gradient measurements^{40,41} and retrospective algorithms based on measurements made with custom pulse sequences.⁴² For instance, previous non-Cartesian multiecho imaging used a prescan to measure gradient delays prior to each scan and demonstrated that gradient timing errors can change even on an individual subject basis.¹⁸ Another limitation is that rosette T_2^* maps are more sensitive to off-resonance-related artifacts than typical Cartesian maps, which can result in a noticeable loss of signal and T_2^* underestimation. This can be seen most readily in the mid-ventricular free wall due to air tissue susceptibility artifacts from the lung. Although susceptibility artifacts are negligible in the septum, care should be taken when performing regional segmentation and global myocardial analysis. Further, although our ungated approach produced images of high quality, reproducibility, and robustness, future efforts should explore incorporating motion directly into the reconstruction model.⁴³ We postulate that this would allow T_2^* to be resolved dynamically across motion states and may prove useful in functional MRI-related physiological studies. Lastly, magnitude-based T_2^* measurements are confounded by intravoxel fat and more sophisticated mapping algorithms should be explored in the future.⁴⁴

Conclusion

This work introduced a clinically useful approach for motion-robust iron quantification using rosette k -sampling and a model-based reconstruction that produces better-quality images and more robust quantification than conventional methods.

Acknowledgments

The authors thank the many helpful colleagues of RSL and MRSRL at Stanford University, the technical staff at Lucile Packard Children's Hospital, and dedicate this work to Mammen Puliyl, MD, Kobe Bryant, and Nipsey Hussle.

References

- Anderson LJ, Holden S, Davis B, et al. Cardiovascular T2-star (T2*) magnetic resonance for the early diagnosis of myocardial iron overload. *Eur Heart J* 2001;22(23):2171-2179.
- Wood JC, Enriquez C, Ghugre N, et al. MRI R2 and R2* mapping accurately estimates hepatic iron concentration in transfusion-dependent thalassemia and sickle cell disease patients. *Blood* 2005;106:1460-1465.
- Ghugre NR, Gonzalez-Gomez I, Butensky E, et al. Patterns of hepatic iron distribution in patients with chronically transfused thalassemia and sickle cell disease. *Am J Hematol* 2009;84(8):480-483.
- Hernando D, Levin YS, Sirlin CB, Reeder SB. Quantification of liver iron with MRI: State of the art and remaining challenges. *J Magn Reson Imaging* 2014;40(5):1003-1021.
- Noetzli LJ, Papudesi J, Coates TD, Wood JC. Pancreatic iron loading predicts cardiac iron loading in thalassemia major. *Blood* 2009;114(19):4021-4026.
- Wood JC. Cardiac iron across different transfusion-dependent diseases. *Blood Rev* 2008;22(Suppl 2):S14-S21.
- Modell B, Khan M, Darlison M, Westwood MA, Ingram D, Pennell DJ. Improved survival of thalassaemia major in the UK and relation to T2* cardiovascular magnetic resonance. *J Cardiovasc Magn Reson* 2008;10:42.
- Ahmad R, Hu HH, Krishnamurthy R. Reducing sedation for pediatric body MRI using accelerated and abbreviated imaging protocols. *Pediatr Radiol* 2018;48(1):37-49.
- Noetzli LJ, Carson SM, Nord AS, Coates TD, Wood JC. Longitudinal analysis of heart and liver iron in thalassemia major. *Blood* 2008;112(7):2973-2978.
- Kirk P, Roughton M, Porter JB, et al. Cardiac T2* magnetic resonance for prediction of cardiac complications in thalassemia major. *Circulation* 2009;120(20):1961-1968.
- Chouliaras G, Berdoukas V, Ladis V, et al. Impact of magnetic resonance imaging on cardiac mortality in thalassemia major. *J Magn Reson Imaging* 2011;34(1):56-59.
- Kellman P, Xue H, Spottiswoode BS, et al. Free-breathing T2* mapping using respiratory motion corrected averaging. *J Cardiovasc Magn Reson* 2015;17(1):3.
- Barrera CA, Otero HJ, Hartung HD, Biko DM, Serai SD. Protocol optimization for cardiac and liver iron content assessment using MRI: What sequence should I use? *Clin Imaging* 2019;56:52-57.
- Jin N, da Silveira JS, Jolly MP, et al. Free-breathing myocardial T2* mapping using GRE-EPI and automatic non-rigid motion correction. *J Cardiovasc Magn Reson* 2015;17:113.
- Glover GH, Pauly JM. Projection reconstruction techniques for reduction of motion effects in MRI. *Magn Reson Med* 1992;28(2):275-289.
- Lustig M, Donoho D, Pauly JM. Sparse MRI: The application of compressed sensing for rapid MR imaging. *Magn Reson Med* 2007;58(6):1182-1195.
- Lee GR, Griswold MA, Tkach JA. Rapid 3D radial multi-echo functional magnetic resonance imaging. *Neuroimage* 2010;52(4):1428-1443.
- Armstrong T, Dregely I, Stemmer A, et al. Free-breathing liver fat quantification using a multiecho 3D stack-of-radial technique. *Magn Reson Med* 2018;79(1):370-382.
- Noll DC. Multishot rosette trajectories for spectrally selective MR imaging. *IEEE Trans Med Imaging* 1997;16(4):372-377.
- Li Y, Yang R, Zhang C, Zhang J, Jia S, Zhou Z. Analysis of generalized rosette trajectory for compressed sensing MRI. *Med Phys* 2015;42(9):5530-5544.
- Schirda CV, Tanase C, Boada FE. Rosette spectroscopic imaging: Optimal parameters for alias-free, high sensitivity spectroscopic imaging. *J Magn Reson Imaging* 2009;29(6):1375-1385.
- Noll DC, Fessler JA, Sutton BP. Conjugate phase MRI reconstruction with spatially variant sample density correction. *IEEE Trans Med Imaging* 2005;24(3):325-336.
- Sutton BP, Noll DC, Fessler JA. Fast, iterative image reconstruction for MRI in the presence of field inhomogeneities. *IEEE Trans Med Imaging* 2003;22(2):178-188.
- Winkelmann S, Schaeffter T, Koehler T, Eggers H, Doessel O. An optimal radial profile order based on the Golden Ratio for time-resolved MRI. *IEEE Trans Med Imaging* 2007;26(1):68-76.
- Larson AC, White RD, Laub G, McVeigh ER, Li D, Simonetti OP. Self-gated cardiac cine MRI. *Magn Reson Med* 2004;51(1):93-102.
- Brodsky EK, Samsonov AA, Block WF. Characterizing and correcting gradient errors in non-Cartesian imaging: Are gradient errors linear time-invariant (LTI)? *Magn Reson Med* 2009;62(6):1466-1476.
- Trzasko J, Manduca A. Highly undersampled magnetic resonance image reconstruction via homotopic l0-minimization. *IEEE Trans Med Imaging* 2009;28(1):106-121.
- Uecker M, Lai P, Murphy MJ, et al. ESPIRiT—An eigenvalue approach to autocalibrating parallel MRI: Where SENSE meets GRAPPA. *Magn Reson Med* 2014;71(3):990-1001.
- Buehrer M, Pruessmann KP, Boesiger P, Kozerke S. Array compression for MRI with large coil arrays. *Magn Reson Med* 2007;57(6):1131-1139.
- Martin Uecker FO, Jonathan Tamir, Dara Bahri, Patrick Virtue, Joseph Cheng, Tao Zhang, Michael Lustig. Berkeley advanced reconstruction toolbox. In: *Proc 23rd Annual Meeting ISMRM, Toronto*; 2015.
- He T, Gatehouse PD, Kirk P, Mohiaddin RH, Pennell DJ, Firmin DN. Myocardial T2* measurement in iron-overloaded thalassemia: An ex vivo study to investigate optimal methods of quantification. *Magn Reson Med* 2008;60(2):350-356.
- Yoshimura K, Kato H, Kuroda M, et al. Development of a tissue-equivalent MRI phantom using carrageenan gel. *Magn Reson Med* 2003;50(5):1011-1017.
- Knobloch G, Colgan T, Wiens CN, et al. Relaxivity of ferumoxytol at 1.5 T and 3.0 T. *Invest Radiol* 2018;53(5):257-263.
- He T. Cardiovascular magnetic resonance T2* for tissue iron assessment in the heart. *Quant Imaging Med Surg* 2014;4(5):407-412.
- Tsai CM, Nishimura DG. Reduced aliasing artifacts using variable-density k-space sampling trajectories. *Magn Reson Med* 2000;43(3):452-458.
- Westwood M, Anderson LJ, Firmin DN, et al. A single breath-hold multiecho T2* cardiovascular magnetic resonance technique for diagnosis of myocardial iron overload. *J Magn Reson Imaging* 2003;18(1):33-39.
- Smith GC, Carpenter JP, He T, Alam MH, Firmin DN, Pennell DJ. Value of black blood T2* cardiovascular magnetic resonance. *J Cardiovasc Magn Reson* 2011;13:21.
- Carpenter JP, He T, Kirk P, et al. On T2* magnetic resonance and cardiac iron. *Circulation* 2011;123(14):1519-1528.
- Alexey Dimov NB, Keigo Kawaji, Timothy Carroll. Retrospective gradient delay correction in multishot, multi-echo rosette acquisition. In: *Proc 27th Annual Meeting ISMRM, Montreal*; 2019.
- Duyn JH, Yang Y, Frank JA, van der Veen JW. Simple correction method for k-space trajectory deviations in MRI. *J Magn Reson* 1998;132(1):150-153.

41. Brodsky EK, Klaers JL, Samsonov AA, Kijowski R, Block WF. Rapid measurement and correction of phase errors from B0 eddy currents: Impact on image quality for non-Cartesian imaging. *Magn Reson Med* 2013;69(2):509-515.
42. Vannesjo SJ, Haeberlin M, Kasper L, et al. Gradient system characterization by impulse response measurements with a dynamic field camera. *Magn Reson Med* 2013;69(2):583-593.
43. Christodoulou AG, Shaw JL, Nguyen C, et al. Magnetic resonance multitasking for motion-resolved quantitative cardiovascular imaging. *Nat Biomed Eng* 2018;2(4):215-226.
44. Reeder SB, Pineda AR, Wen Z, et al. Iterative decomposition of water and fat with echo asymmetry and least-squares estimation (IDEAL): Application with fast spin-echo imaging. *Magn Reson Med* 2005;54(3):636-644.